Astronomy & Astrophysics manuscript no. output
July 27, 2025

Asteroseismology of the ZZ Ceti star WD 1310+583 using the Transiting Exoplanet Survey Satellite

Zsófia Bognár[1]⋆, Murat Uzundag[2], Francisco C. De Gerónimo[3,4], Alejandro H. Córsico[3,4], James Munday[5], Ádám Sódor[1]

[1] Konkoly Observatory, HUN-REN Research Centre for Astronomy and Earth Sciences, MTA Centre of Excellence, H-1121 Budapest, Konkoly Thege Miklós út 15-17, Hungary
[2] Institute of Astronomy, KU Leuven, Celestijnenlaan 200D, B-3001 Leuven, Belgium
[3] Instituto de Astrofísica de La Plata, IALP (CCT La Plata), CONICET-UNLP, Argentina
[4] Grupo de Evolución Estelar y Pulsaciones. Facultad de Ciencias Astronómicas y Geofísicas, Universidad Nacional de La Plata, Paseo del Bosque s/n, (1900) La Plata, Argentina
[5] Department of Physics, Gibbet Hill Road, University of Warwick, Coventry CV4 7AL, United Kingdom

ABSTRACT

Context. The Transiting Exoplanet Survey Satellite (TESS) observed many pulsating ZZ Ceti white dwarf stars, but the star presented in this paper shows a particularly large number of pulsational frequencies, which provides an excellent opportunity for detailed asteroseismic investigations.
Aims. Light curve analysis of the star to determine its pulsaional frequencies, then determination of the main physical parameters of WD 1310+583 utilising the tools of asteroseismology.
Methods. Fourier analyses of the TESS light curves, selection of possible pulsational modes, spectroscopical analysis based on data collected with the Cosmic Origins Spectrograph of the Hubble Space Telescope, providing asteroseismic analyses.
Results. Determination of the main physical parameters of the star: $M_* = 0.632\,M_\odot$, $T_{\rm eff} = 11\,702$ K. The asteroseismic distance derived is 27.75 pc, which is in good agreement with the geometric distance 30.79 pc calculated from Gaia astrometry.

Key words. techniques: photometric – stars: individual: WD 1310+583 – stars: interiors – stars: oscillations – white dwarfs

1. Introduction

ZZ Ceti stars, also known as DAV stars, are pulsating white dwarfs with hydrogen-dominated atmospheres. These stars exhibit low-amplitude multiperiodic brightness variations caused by nonradial g-mode oscillations with periods ranging from 100 to 1500 seconds. These pulsations are driven by a combination of the $\kappa - \gamma$ mechanism, operating within the partial ionisation zone of hydrogen (Dolez & Vauclair 1981; Winget et al. 1982), and the convective driving mechanism (Brickhill 1991; Goldreich & Wu 1999). With effective temperatures spanning 10 500 to 13 000 K, ZZ Ceti stars are confined to a well-defined region in the Hertzsprung–Russell diagram known as the ZZ Ceti instability strip.

As these stars cool across the instability strip, their pulsational properties vary systematically. Near the blue (hot) edge, they exhibit a smaller number of pulsation modes with lower amplitudes and shorter periods. Toward the red (cool) edge, the number of detectable modes increases, their amplitudes grow, and the pulsations become less stable, often showing amplitude and frequency variations on timescales of days to weeks (see e.g section 6 in Fontaine & Brassard 2008). Intriguingly, many cool ZZ Ceti stars also display episodic outbursts, characterised by brief and irregular increases in stellar brightness (see Bell et al. 2015, 2016, 2017; Bognár et al. 2023) and Hermes et al. (2015), which may provide insight into the interaction between pulsation and convection.

ZZ Ceti stars are invaluable astrophysical laboratories for investigating the physics of dense matter under extreme conditions. Their small size (approximately Earth-like) and high surface gravity ($\log g \sim 8$) result in strongly stratified atmospheres, where heavier elements settle below a hydrogen or helium layer due to gravitational separation. These characteristics make them ideal for asteroseismology, a technique that uses observed pulsation periods to infer the star's internal structure, chemical composition, and rotational properties. Such studies contribute to understanding stellar evolution and the formation of compact objects (Winget & Kepler 2008; Fontaine & Brassard 2008; Althaus et al. 2010; Córsico et al. 2019; Córsico 2020).

Recent advances in space-based photometry, particularly with the Transiting Exoplanet Survey Satellite (TESS; Ricker et al. 2015), have revolutionised the study of ZZ Ceti stars. TESS provides high-precision, high-cadence observations, enabling detailed frequency analyses and the detection of new pulsation modes, even in stars previously deemed observationally challenging. This has opened new avenues for understanding the global properties of white dwarfs and the underlying physics driving their pulsations (Bell et al. 2019; Bognár et al. 2020).

TESS was launched on 18 April 2018, and the main goal of the mission was to find exoplanets at bright nearby stars with the transit method. However, observations of pulsating stars are also allowed by the time-sampling of the measurements. During the first two years of the mission, it provided 30-minute (long) cadence full-frame images (FFIs) from almost the entire sky and 120-second (short) cadence observations on selected targets. The time sampling of these short-cadence observations allowed us

⋆ e-mail: bognar.zsofia@csfk.org

to study the light variations of compact pulsators. Fortunately, the observations are not finished after the two-year primary mission but continue in TESS extended missions. In the first extended mission, the full-frame image cadence was reduced to 10 minutes, and a new, 20-second ultra-short cadence mode was implemented. The latter modification was welcomed, considering the short periods seen in compact pulsators. The second extended mission is expected to last three years (2022–2025). In this mission, TESS shortened the FFI cadence to 200 seconds and maintained the cadence modes of 20 seconds and 2 minutes for preselected targets [1]. Considering the compact variables: (pre)white dwarf and hot subdwarf stars, the corresponding activities are coordinated by the TESS Asteroseismic Science Consortium (TASC) Compact Pulsators Working Group WG#8.

The brightness variations of the ZZ Ceti star WD 1310+583 were independently discovered by Gentile Fusillo et al. (2018) and Bognár et al. (2018). The latter study presents photometric investigations conducted at the Konkoly Observatory (Hungary). Seven independent modes were identified on the basis of the data sets. In the study by Gentile Fusillo et al. (2018), two possible pulsation frequencies were published as a result of their analysis.

In this paper, we focus on the TESS measurements of WD 1310+583. First, we analysed the spectrocopic data available on WD 1310+583, then we present the TESS data sets to identify the pulsation modes of this star. Using these findings, we then performed an asteroseismic investigation to constrain its global parameters and internal structure.

2. Spectroscopic analysis

In the following, we present the results of the system parameters of a double-degenerate fit to the spectra obtained on WD 1310+583.

2.1. Method

WD 1310+583 has been independently suggested as a double degenerate source based on spectroscopic or hybrid (photometric, spectroscopic plus astrometric data) fits using ultraviolet (Gentile Fusillo et al. 2018) and optical (Munday et al. 2024) spectroscopy. Munday et al. (2024) found little radial velocity variability, indicating that the source is likely a wide double white dwarf binary star system. At the time of writing, precise *Gaia* parallax measurements were not available to Gentile Fusillo et al. (2018) and the authors chose to fix the surface gravity of both stars to $\log(g) = 8.0$ dex when producing atmospheric parameters of the two stars. With that in mind and to obtain an improved spectroscopic solution to the ultra-violet data, we decided to refit their Hubble Space Telescope Cosmic Origins Spectrograph (HST COS) spectrum with new information at hand, utilising all-sky photometry and *Gaia* parallaxes to give absolute flux measurements.

We used the WD-BASS pipeline (Munday et al. 2024) with Pan-STARRS all-sky photometry (Chambers & Pan-STARRS Team 2018, filters *grizy*), the Sloan Digital Sky Survey (filters *ugriz*) DR16 (Ahumada et al. 2020), and the *Gaia* DR3 parallax of $\pi = 32.48 \pm 0.25$ mas. We fit the wavelength range of 1200–1930 Å, trimming the very low signal-to-noise data. We mask geocoronal lines between vacuum wavelengths 1206–1226 Å, 1295–1315 Å and also within 1 Å of all entries supplied in the line list of Sahu et al. (2023) to ignore any potential undesired photospheric/interstellar flux contribution.

Synthetic spectra were obtained by interpolating the 3D local thermodynamic equilibrium grids of Tremblay et al. (2013, 2015) for DA white dwarfs, which are based on the line profiles of Tremblay & Bergeron (2009). The hotter star, which dominates the flux, has Balmer absorption lines and is clearly a DA, but the spectral class of the secondary star is unknown since it exhibits no unique spectral lines. Hence, the dimmer companion could be a helium-atmosphere DC, and in testing this DA+DC combination, we interpolate synthetic spectra from Cukanovaite et al. (2021). The temperature, surface gravity, and radial velocity of the two stars and the parallax of the system were independent variables in the fitting. We used a mass-temperature-radius relationship from the hydrogen-rich evolutionary sequences of Bédard et al. (2020) for a DA and the He-rich evolutionary sequences of Bédard et al. (2020) for a DC to obtain stellar radii and calculate the luminosity of each star. Observations were scaled from an Eddington flux to an observed flux using the reciprocal of the parallax as the distance in parsecs, with an extinction coefficient of $E(B-V)=A_V/R_V = 0.01/3.1$ applied to redden the synthetic spectra (Gentile Fusillo et al. 2021). No spectrum normalisation is applied; the observed flux in physical units is fitted in both the HST COS spectrum and the all-sky photometry with a common parallax measurement to each dataset. A Gaussian prior was placed on the fitted parallax using the parallax and the error reported in *Gaia* DR3.

Table 1. Physical parameters of the different spectroscopic fits. The errors are statistical errors from the fits, thus under-predicted.

DA+DA fit	
T_1 =	11670 ± 10 K
$\log g_1$ =	8.13 ± 0.01 dex
T_2 =	8240 ± 60 K
$\log g_2$ =	8.09 ± 0.01 dex
Fitted Parallax =	31.75 ± 0.17 mas
DA+DC fit	
T_1 =	11650 ± 10 K
$\log g_1$ =	8.12 ± 0.01 dex
T_2 =	7540 ± 40 K
$\log g_2$ =	7.78 ± 0.01 dex
Fitted Parallax =	31.56 ± 0.17 mas

2.2. System parameters

The best-fit solutions are shown in Fig. 1 and Fig. 2, respectively, while the physical parameters of the different solutions can be seen in Table 1.

3. Light curve analyses of the TESS observations

TESS measured the star in 120-second short-cadence mode in these sectors: 15, 16, 22, 48, 49, 75, 76. Measurements are also available in 20-second ultra-short cadence mode, but we did not see peaks above the Nyquist frequency of the 120-second measurements. So, we examine the 120-second measurements more closely.

First, we performed frequency analyses for sectors s15s16, s22, s48s49, and s75s76 using the photometric module of the Frequency Analysis and Mode Identification for Asteroseismology (FAMIAS) software package (Zima 2008). As seems, we treat

[1] https://heasarc.gsfc.nasa.gov/docs/tess/docs/Guide-to-TESS-for-EM-planning.pdf

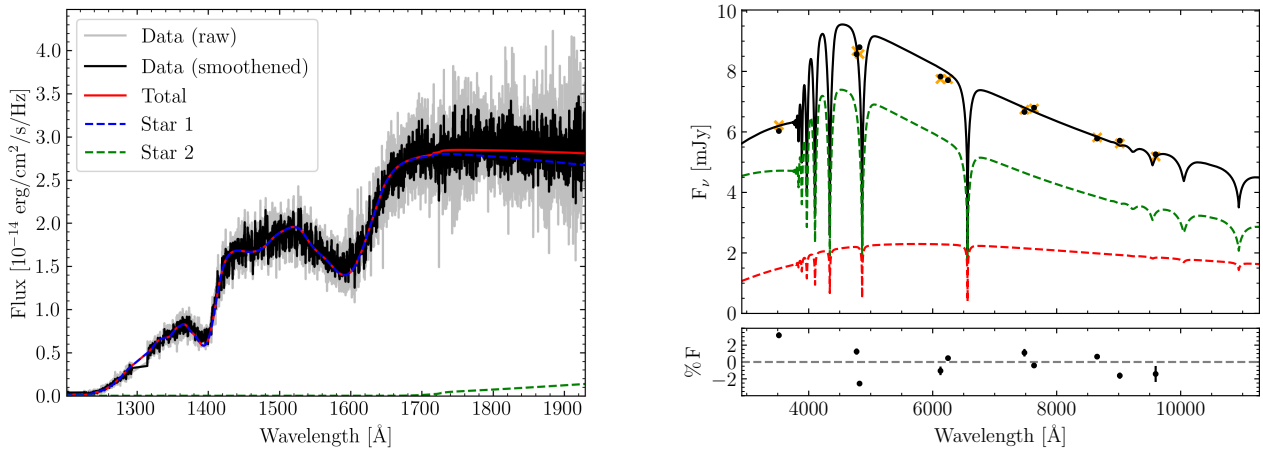

Fig. 1. DA+DA fit presented in the panels of the figure. For more details, see Sect. 2.

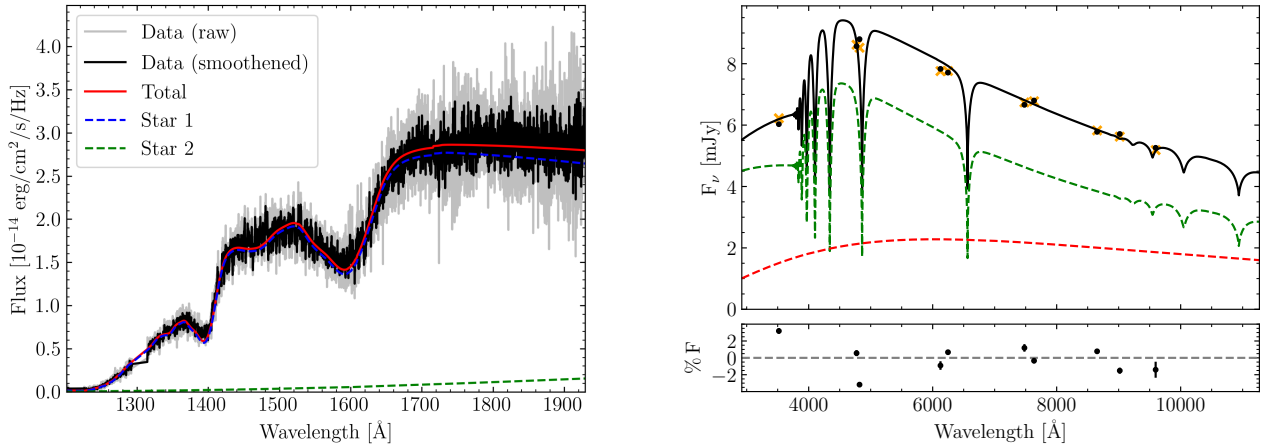

Fig. 2. DA+DC fit presented in the panels of the figure. For more details, see Sect. 2.

the data of the neighbouring sectors jointly. For frequency analyses, we set the significance limit at 0.1% False Alarm Probability (FAP). We created a table of the observed peaks in the different sectors and considered the peaks that are approximately at the same frequency in the different data sets as the same frequency. Then, after we identified the common frequencies and their amplitudes provided by the analyses, we calculated the amplitude-averaged period value for each frequency. We also checked for the presence of linear combinations in each data set.

There are groups of peaks above about 700 s, and we considered the one with the highest amplitude as the representative frequency of the given frequency group.

Table 2 summarises the journal of observations, while Table 3 lists the frequencies, periods, and amplitudes of the peaks detected by the analysis of the data sets from the different sectors.

The comparison of the Fourier spectra of the different segments of the light curve is shown in Fig. 3.

4. Rotational multiplets

The equation we used to calculate the rotation period of a star is as follows.

$$\delta f_{k,l,m} = m(1 - C_{k,l})\Omega, \tag{1}$$

where k, l, and m are the radial order, horizontal degree, and azimuthal order of the non-radial pulsation mode, respectively. The coefficient $C_{k,l}$ can be calculated as $C_{k,l} \approx 1/\ell(\ell+1)$. This relation is valid for high-overtone ($k \gg \ell$) g-modes. Ω is the (uniform) rotational frequency.

Examining the frequencies listed in Table 3 reveals the presence of possible rotational triplet and doublet frequencies separated by approximately 5 μHz. A total of eight doublets and two triplets were identified, as summarised in Fig. 4 and Table 4. Assuming that all are $l = 1$ modes and that the average frequency separation is 4.9 μHz, the star's rotational period is calculated to be P = 1.18 d. This value is in good agreement with the hour-to-day rotation periods typically observed in pulsating white dwarf stars.

Table 2. Journal of observations of WD 1310+583. *TIC ID* refers to the TESS Input Catalog identifier of the object, *N* is the number of data points after cleaning the light curve, δT is the total length of the data sets including gaps, and *Sect.* is the serial number of the sector(s) in which the star was observed. The start time in BJD is the time of the first data point in the data set. The *CROWDSAP* keyword represents the ratio of the target flux to the total flux in the TESS aperture. We note that here we list the CROWDSAP value from the first TESS run.

Object	TIC ID	Start time (BJD-2 457 000)	*N*	δT (d)	*G* mag	Sect. (Cadence)	CROWDSAP
WD 1310+583	157271533	1711.362	29 058	51.2	14.1	15–16 (120 s)	0.99
		1900.094	16 326	26.4		22 (120 s)	
		2610.234	28 155	54.1		48–49 (120 s)	
		3339.788	21 531	55.0		75–76 (120 s)	

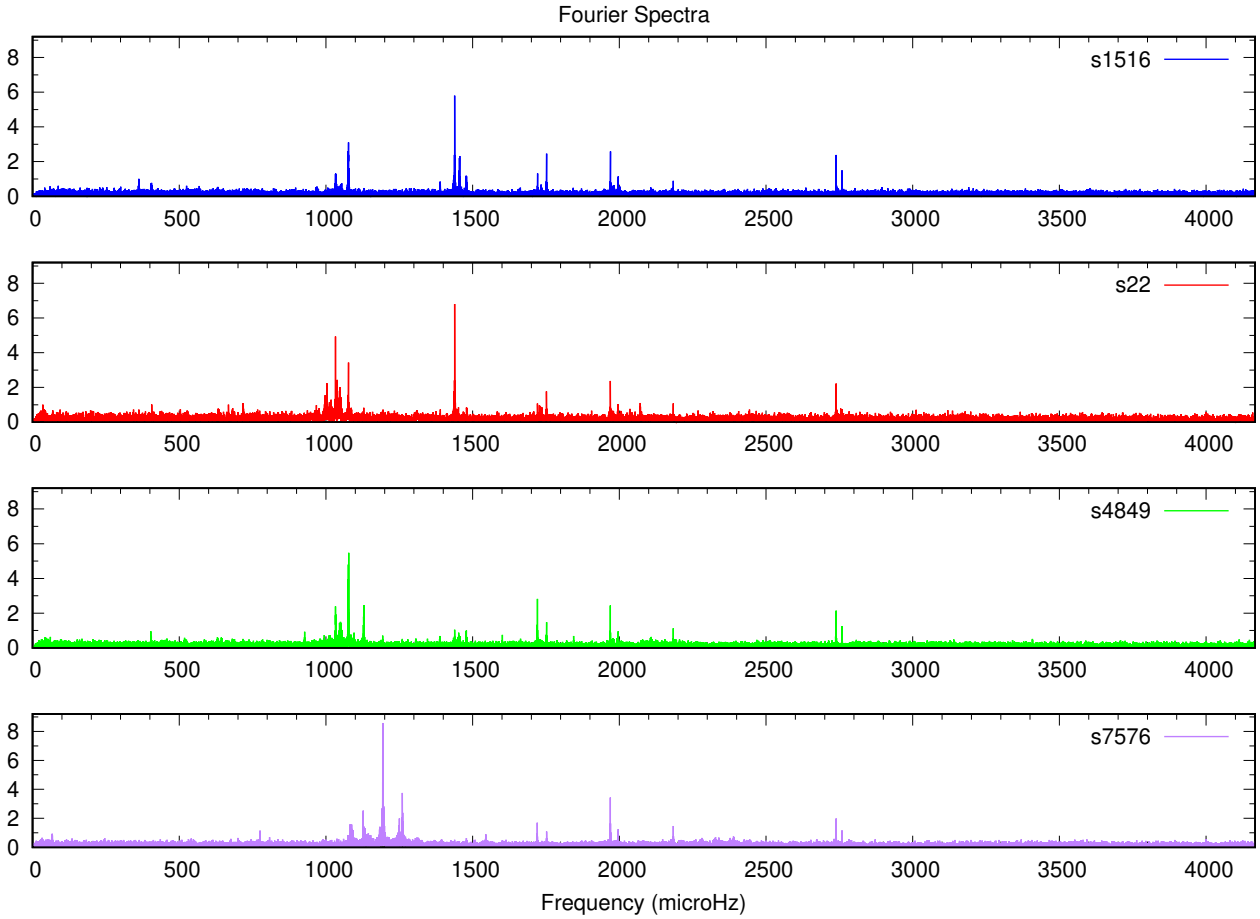

Fig. 3. Fourier spectra of the different light curve segments

5. Period spacing tests

Here, our primary goal is to deepen our understanding of stellar structure, particularly the mass of the observed object. We note that the photometric and spectroscopic masses are in good agreement, as shown in Table B.1. of the following work: Calcaferro et al. (2024). The mean period spacing serves as an indicator of the stellar mass. We conducted several tests. Using a subset of the periods listed in Table 3, we searched for a characteristic period spacing using Kolmogorov-Smirnov (K-S; Kawaler 1988) and inverse variance (I-V; O'Donoghue 1994) significance tests. In the K-S test, the quantity Q represents the probability that the observed periods are randomly distributed. A characteristic period spacing in the period spectrum would manifest itself as a minimum in Q. Meanwhile, in the I-V test, a maximum indicates the presence of a constant period spacing. Another widely recognised approach to identifying a characteristic spacing value is performing a Fourier analysis on a Dirac comb constructed directly with periods (e.g. Winget et al. 1991; Handler et al. 1997).

Fig. 5 shows the results of applying the statistical tests to a subset of 11 periods detected in WD 1310+583. These periods are marked with an asterisk in Table 3. The three tests reveal a clear period spacing of 40.58 s, which can be associated with modes that have $\ell = 1$. The presence of a spacing of $\sim$ 20 seconds is also observed in the three tests. This corresponds to the subharmonic of the spacing ($\Delta\Pi/2$). We refine the value of the period spacing of $\sim$ 40.6 s by plotting the 11 periods mentioned in terms of a relative radial order (see Fig. 6). Using a linear least-squares fit, we obtain $\Delta\Pi_{\ell=1} = 40.51 \pm 0.14$ s. From the residuals of the period distribution relative to the mean period spacing (lower panel of Fig. 6), the signals of mode trapping in the period spectrum of WD 1310+583 are apparent. The discovery of the period spacing $\Delta\Pi_{\ell=1}$ allows the harmonic degree $\ell = 1$ to be assigned to the 11 periods that make up the sequence,

Table 3. Frequency, period, and amplitude values determined from the TESS data sets. Only three periods are from the literature, which are indicated in the fourth column. Where similar frequencies were found in multiple TESS data sets, their amplitude-averaged period is listed in the table. Periods that form a regular pattern of $\ell = 1$ modes with constant period spacing are marked with an asterisk (see Sect. 5). In cases where a significant frequency was found in only one data set, the sector number is indicated in the fourth column. The fifth column notes if the given frequency was identified as a linear combination in any data set.

	f [μHz]	P [s]	A [mma]	Comments	Lin. comb.
f_{01}	634.0	1577.3	6.6	Bognár et al. (2018)	
f_{02}	668.0	1497.0	1.08	only in s22	
f_{03}	717.4	1394.0	1.07	s22	
f_{04}	927.3	1078.4*	0.98	s4849	
f_{05}	963.0	1038.4*	7.0	Bognár et al. (2018)	
f_{06}	997.2	1002.8	1.70	s22	
f_{07}	1003.0	997.1*	2.41	s22	
f_{08}	1012.6	987.5	1.12	s22	
f_{09}	1017.8	982.5	1.44	s22	
f_{10}	1032.7	968.4	2.98		
f_{11}	1039.2	962.2	1.86		
f_{12}	1044.8	957.2	1.41		
f_{13}	1048.6	953.6*	1.95		
f_{14}	1076.9	928.6	3.69		
f_{15}	1082.6	923.7	1.48	s7576	
f_{16}	1087.8	919.3*	2.08	s7576	
f_{17}	1093.4	914.5	0.99		
f_{18}	1126.9	887.4	2.37	s7576	
f_{19}	1129.7	885.2	1.86	s7576	
f_{20}	1133.9	881.9	1.31	s7576	
f_{21}	1144.5	873.8*	1.12	s7576	
f_{22}	1149.5	869.9	0.91	s7576	
f_{23}	1183.9	844.7	1.31	s7576	
f_{24}	1193.9	837.6*	10.45	s7576	
f_{25}	1196.6	835.7	2.24	s7576	
f_{26}	1250.3	799.8	2.67	s7576	
f_{27}	1260.3	793.4*	3.94	s7576	
f_{28}	1389.1	719.9	0.86	s1516	
f_{29}	1435.0	696.9	0.97	s1516	
f_{30}	1438.9	695.0	4.74		
f_{31}	1454.6	687.5	1.46		
f_{32}	1478.9	676.2*	1.08		
f_{33}	1601.3	624.5	0.82	s4849	
f_{34}	1727.9	578.7	1.05	s22	
f_{35}	1751.9	570.8	1.87		
f_{36}	1844.2	542.2	0.78	s4849	
f_{37}	1969.4	507.8*	2.94		
f_{38}	1996.0	501.0	1.21		
f_{39}	2558.3	390.9*	–	Gentile Fusillo et al. (2018)	
f_{40}	2739.0	365.1	2.39		
f_{41}	2759.0	362.4	1.40		
	362.2	2761.2	1.01	s1516	yes (s1516)
	404.8	2470.2	0.98		yes (s1516, s22)
	775.2	1290.0	1.38	s7576	yes (s7576)
	967.5	1033.6	1.07	s22	yes (s22)
	1544.9	647.3	1.04	s7576	yes (s7576)
	1720.8	581.1	1.89		yes (s22)
	2071.0	482.9	1.32		yes (s22)
	2183.9	457.9	1.29		yes (s1516)
	2387.7	418.8	0.85	s7576	yes (s7576)

allowing to place strong constraints to fits of individual periods (see Section 6.2).

6. Asteroseismology

All of our efforts to determine the independent pulsation modes were for to provide these modes for the asteroseismic analysis of the star presented in the next sections.

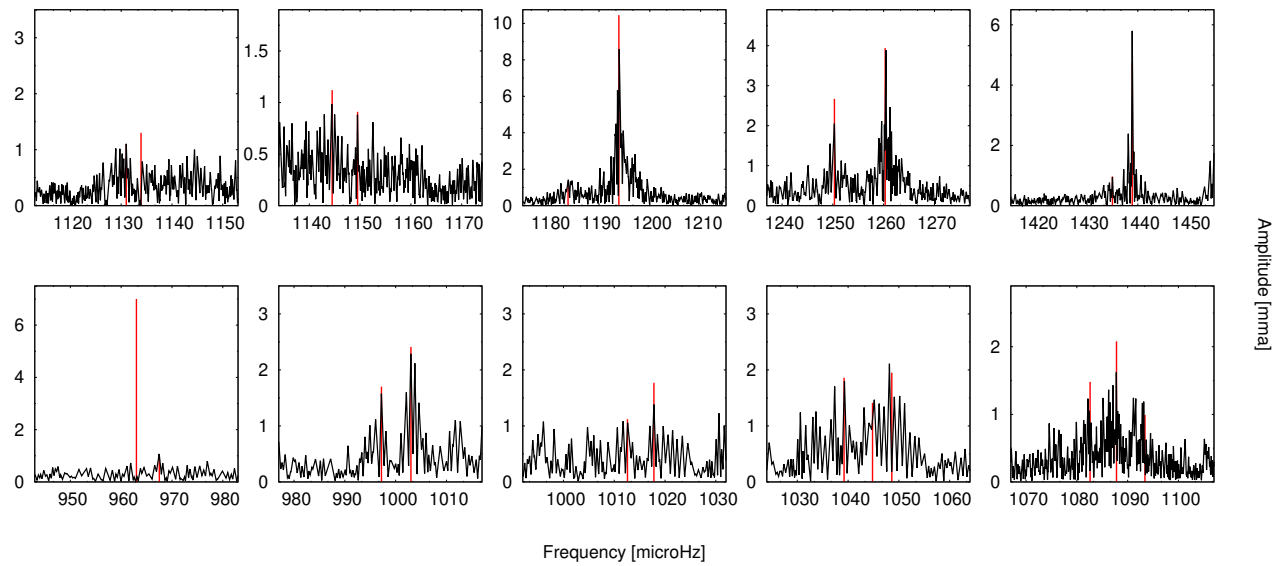

Fig. 4. Fourier spectra of possible rotational triplet and doublet frequencies. We note that the Fourier spectra have already been pre-whitened up to the highest-amplitude peak of the multiplet, but in many cases, the lower-amplitude peaks become more clearly visible only after further pre-whitening.

Table 4. Possible rotational triplet and doublet frequencies. We also mark the frequency differences in the second column.

f [μHz]	δf [μHz]
963.0	
967.5	4.5
997.2	
1003.0	5.8
1012.6	
1017.8	5.2
1039.2	
1044.8	5.6
1048.6	3.8
1082.6	
1087.8	5.2
1093.4	5.6
1129.7	
1133.9	4.2
1144.5	
1149.5	5.0
1183.9	
1193.9	10.0
1250.3	
1260.3	10.0
1435.0	
1438.9	3.9

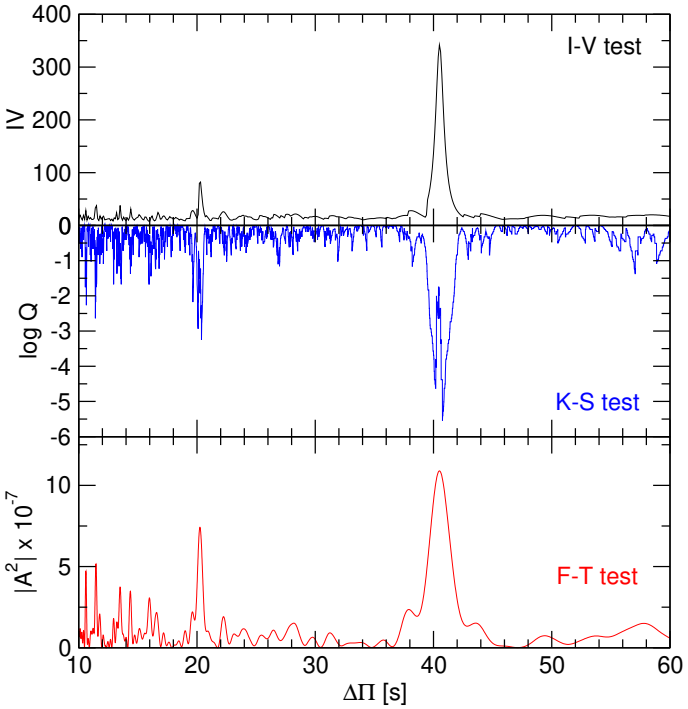

Fig. 5. Results of the inverse variance (I-V, black), Kolmogorov-Smirnov (K-S, blue), and Fourier Transform (F-T, red) statistical tests applied to a subset of 11 periods marked with asterisks in Table 3. The three tests point to the existence of a period spacing of 40.58 s in WD 1310+583, which can be associated to $\ell = 1$ modes. The presence of the subharmonic of this spacing at $\sim$ 20 seconds is also apparent.

6.1. The stellar mass of WD 1310+583 as predicted by the observed period spacing

A practical approach to estimate the stellar mass of pulsating WD stars involves comparing the observed period spacing ($\Delta\Pi$)

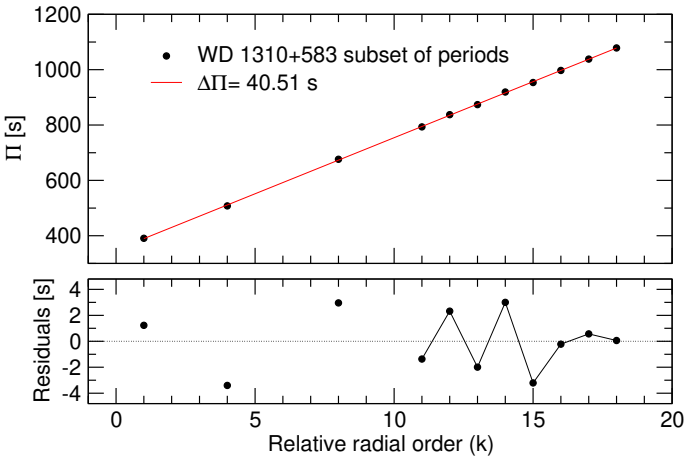

Fig. 6. Upper panel: linear least-squares fit to the 11 periods of WD 1310+583 marked with asterisks in Table 3. The derived period spacing from this fit is $\Delta\Pi_{\ell=1} = 40.51$ s. Lower panel: residuals of the period distribution relative to the mean period spacing, revealing signals of mode trapping in the period spectrum of WD 1310+583. Modes with a consecutive radial order are connected with thin black lines.

with the average of the calculated period spacings ($\overline{\Delta\Pi_k}$) (Córsico et al. 2019). The average is determined using the formula $\overline{\Delta\Pi_k} = (n-1)^{-1} \sum_k \Delta\Pi_k$, where the "forward" period spacing ($\Delta\Pi_k$) is defined as $\Delta\Pi_k = \Pi_{k+1} - \Pi_k$ (with k representing the radial order) and n is the number of computed periods that fall within the range of observed periods. It is important to note that this method for determining stellar mass depends on the spectroscopic effective temperature, and the results are inevitably influenced by the uncertainties associated with $T_{\rm eff}$. The method mentioned leverages the fact that, in general, the period spacing of pulsating WD stars is mainly influenced by stellar mass and effective temperature, with only a minor dependence on the thickness of the He envelope for DBV stars or the O/C/He envelope for GW Vir stars (see, e.g., Tassoul et al. 1990). However, this technique cannot be *directly* applied to DAV stars for mass estimation, as the period spacing in these stars is influenced by $M_\star$, $T_{\rm eff}$, and the mass of the H envelope $M_{\rm H}$, with similar sensitivity, leading to multiple combinations of these three parameters that yield the same period spacing. Therefore, we can only provide a possible range of stellar masses for WD 1310+583 based on the period spacing.

We calculated the mean of the period spacings for $\ell = 1$, denoted as $\overline{\Delta\Pi_k}$, employing the LP-PUL pulsation code (Córsico & Althaus 2006), in terms of the effective temperature across all considered stellar masses and H-envelope thicknesses (see Table 4 of Uzundag et al. 2023). The analysed period range was established between 300 and 1600 seconds, encompassing the typical periods observed in the target star WD 1310+583. The effective temperature of WD 1310+583 according to this work (see Sect. 2.2) is $T_{\rm eff} = 11\,660 \pm 163$ K on average. However, there are other measurements of $T_{\rm eff}$ for this DAV star in the literature, such as $T_{\rm eff} = 10\,131 \pm 260$ K (Leggett et al. 2018), $T_{\rm eff} = 10\,313 \pm 111$ K (O'Brien et al. 2024), $T_{\rm eff} = 11\,617 \pm 70$ K (Gentile Fusillo et al. 2018), and $T_{\rm eff} = 11\,600 \pm 200$ K (Munday et al. 2024). In particular, the value of $T_{\rm eff}$ derived in the present study is almost the same as the values derived by Gentile Fusillo et al. (2018) and Munday et al. (2024). As there is no definitive effective temperature measurement available for this star, we used multiple estimates to cover the possible range of $T_{\rm eff}$. The results are illustrated in Fig. 7, showing $\overline{\Delta\Pi_k}$ for various stellar masses (specified at the top right corner of each panel), represented by curves with different thicknesses corresponding to the diverse $M_{\rm H}$ values. To enhance clarity, we only labelled the extreme H-envelope thickness values for each stellar mass, using thick and thin black curves. The position of WD 1310+583, marked by a small circle with error bars, was examined with three spectroscopic effective temperature values: $T_{\rm eff} = 10\,131 \pm 260$ K (Leggett et al. 2018), $T_{\rm eff} = 10\,313 \pm 111$ K (O'Brien et al. 2024), representative of most of the $T_{\rm eff}$ determinations, which point to low effective temperatures, and $T_{\rm eff} = 11\,660 \pm 163$ K (this paper), along with a period spacing of $\Delta\Pi = 40.51 \pm 0.14$ s.

Upon analysis of the plot, we infer that, based on the period spacing and $T_{\rm eff}$, the stellar mass of WD 1310+583 likely falls between 0.609 $M_\odot$ (with a thick H envelope of $\log(M_{\rm H}/M_\star) = -4.02$) and 0.877 $M_\odot$ (with a very thin H envelope of $\log(M_{\rm H}/M_\star) = -8.37$) if the effective temperature is high (green dot in Fig. 7). In contrast, if the effective temperature of WD 1310+583 is lower (as indicated by the red and blue dots in Fig. 7), then the stellar mass would probably exceed 0.770$M_\odot$ with a thick envelope of H ($\log(M_{\rm H}/M_\star) = -4.70$). In summary, based on the period spacing and effective temperature, the stellar mass of WD 1310+583 would be larger than $\sim 0.60 M_\odot$.

6.2. Asteroseismic period fits

In this section, our aim is to find an evolutionary model that best matches the theoretical periods with the individual pulsation periods detected for WD 1310+583. The quality of the fit is assessed by evaluating the quality function defined as follows:

$$\chi^2(M_\star, M_H, T_{\rm eff}) = \frac{1}{N} \sum_{i=1}^{N} \min[(\Pi_{\rm i}^{\rm O} - \Pi_{\rm k}^{\rm th})^2], \quad (2)$$

Here, N represents the number of detected modes, $\Pi_i^{\rm O}$ are the observed periods and $\Pi_k^{\rm th}$ are the theoretically computed periods (where k is the radial order). The best-fitting model is chosen by identifying the minimum value of χ^2.

We use the same grid of CO-core WD models as in Uzundag et al. (2023), which contemplate evolutionary sequences of stellar masses in the range $0.525 \leq M_\star/M_\odot \leq 0.877$, with effective temperature $10\,000\,{\rm K} \leq T_{\rm eff} \leq 13\,000\,{\rm K}$, and varying the total hydrogen content $-9 \lesssim \log(M_{\rm H}/M_\star) \lesssim -4$.

For the period-to-period fit, we examined the frequency spectrum of WD 1310+583 and used the confirmed triplets and those consecutive overtones derived as $l = 1$ as input priors, see Table 3 and 4. We considered the central components (with $m = 0$), specifically the 8 observed periods (793.4, 837.6, 873.8, 919.3, 953.6, 997.1, 1038.4, and 1078.4 s), which were assigned $\ell = 1$ for the analysis. The most important stellar parameters of our solutions are shown in Table 5. We found solutions compatible with the spectroscopic determinations for $T_{\rm eff}$ and $\log g$, as well as the astrometric distance provided by *Gaia* (see the next section). Based on the results of our best-fit models, it is more likely that WD J1310+583 has a thick H-envelope. The more massive solution exhibits a significant discrepancy with our spectroscopic determination of $\log g$ and the *Gaia* distance; therefore, we discard this model as a possible solution, despite it providing the best agreement between the theoretical and observed periods.

Since Solution 3 provides a more accurate fit when compared to our spectroscopic values of effective temperature and surface gravity, and the mass determination aligns with the results from the mean period spacing analysis, we select this solution as our

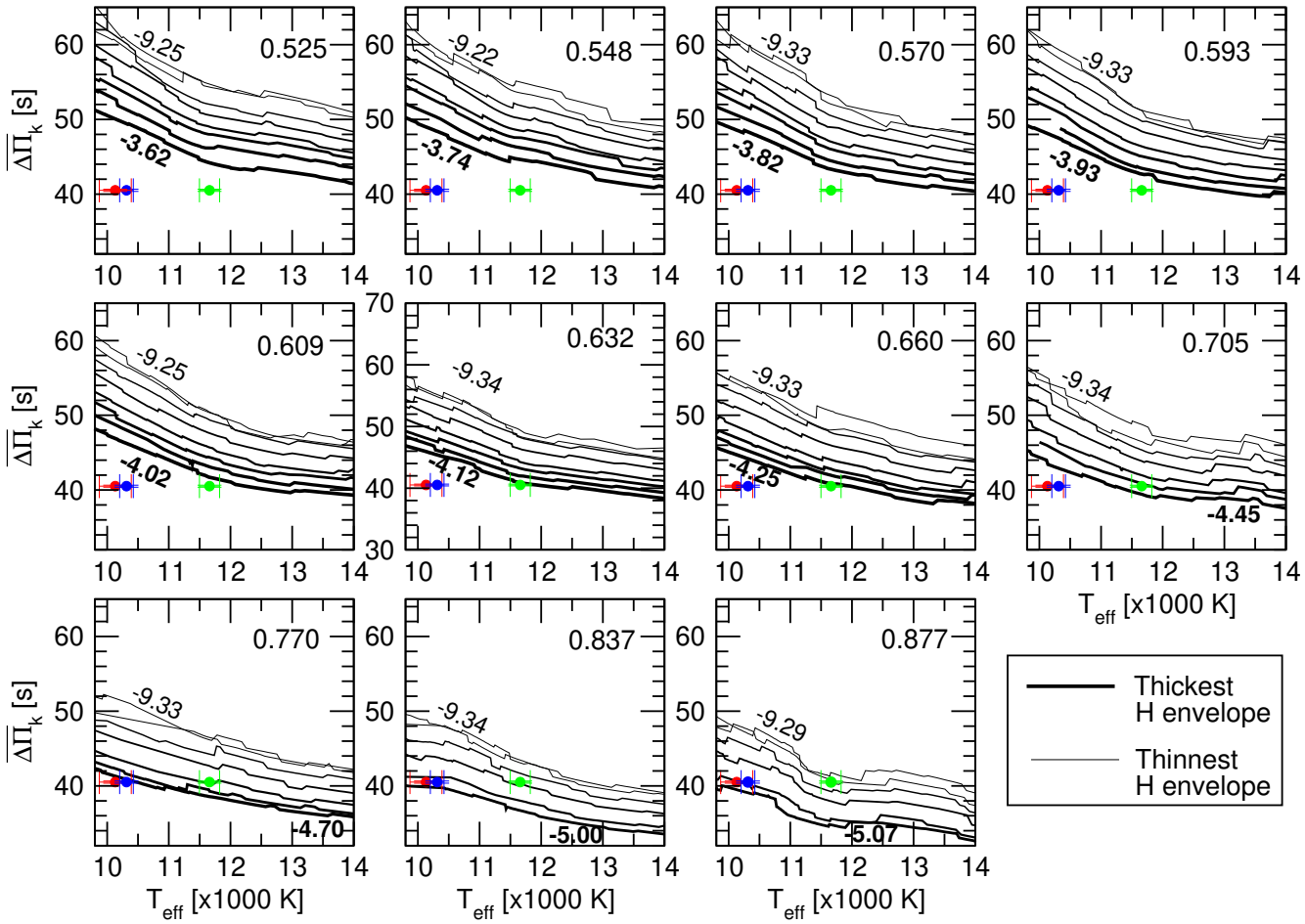

Fig. 7. Average of the computed dipole ($\ell = 1$) period spacings, $\overline{\Delta\Pi_k}$, in terms of the effective temperature, for different stellar masses in solar units (numbers at the top right corner of each panel) and thicknesses of the H envelope (see Table 4 of Uzundag et al. 2023, for the specific values of $\log(M_H/M_\star)$) drawn with different colors. In each panel, we include numbers along two curves, which correspond to the value of $\log(M_H/M_\star)$ for the thickest and the thinnest H envelopes for each stellar mass value. The location of WD 1310+583 is emphasized with an circle with error bars with effective temperatures $T_{eff} = 10\,131 \pm 260$ K (red symbol; Leggett et al. 2018), $T_{eff} = 10\,313 \pm 111$ K (blue symbol; O'Brien et al. 2024), and $T_{eff} = 11\,660 \pm 163$ K (green symbol; section 2.2 of this work), and a period spacing $\Delta\Pi = 40.51 \pm 0.14$ s (Section 5).

Table 5. Parameters of the best-fit models

Model #	$M_\star$ ($M_\odot$)	$\log g$ (cm s^{-2})	T_{eff} (K)	$\log\left(\frac{M_H}{M_\star}\right)$	χ^2	$\ell = 1$	d (pc)
1	0.609	8.03	11 441	-4.02	25.82	21	27.65
2	0.837	8.39	11 147	-5.35	25.30	19	20.74
3	0.632	8.06	11 702	-5.41	27.29	22	27.75

best-fit model. We fitted 22 dipole modes with radial order k in the range [6:21], and the remaining modes being quadrupoles with $k \in$ [11:57] with a quality function value of $\sigma = 5.19$. A complementary analysis was conducted using the set of 11 $\ell = 1$ modes obtained by period spacing analysis, as discussed in Section 5. This approach yields the same asteroseismic model, although it results in a slightly poorer quality function, with a value of $\sigma = 5.45$.

We computed the Bayes Information Criterion (BIC, Koen & Laney 2000):

$$\mathrm{BIC} = N_p \left(\frac{\log N}{N}\right) + \log \sigma^2, \quad (3)$$

that give a global indicator of the quality of our asteroseismic fit, accounting for the free parameters and the value of the quality function. Here N_p is the number of free parameters of the models, N is the number of observed periods to match, and σ is the value of the quality function. The smaller the BIC value, the better the quality of the fit. This criterion introduces a penalty term for an excess in the number of parameters in the model. In our case, $N_p = 3$ (stellar mass, effective temperature, and thickness of the H envelope), $N = 41$ and $\sigma^2 = 27$. We obtain BIC = 1.54, which means that our fit is good.

6.3. Asteroseismic distance

Based on the stellar parameters derived from our best-fit model, we estimate the asteroseismic distance to be WD 1310 + 583. Using the effective temperature and the logarithm of surface gravity, we calculated the absolute magnitude in the *Gaia G* band

(Koester, personal communication). For the solution with a mass of 0.632 $M_\odot$, we find that the absolute magnitude is M_G = 11.85 mag. From the apparent magnitude obtained by *Gaia* Data Release 3 (DR3) Archive[2] for WD 1310+583 (m_G = 14.07 mag), we obtain an asteroseismic distance of d =27.75 pc. An essential part of validating our best-fit asteroseismic model is comparing the asteroseismic distance with the distance obtained directly from *Gaia*. We found an excellent match with the *Gaia* distance (Bailer-Jones et al. 2021), which reports of $d = 30.79 \pm 0.2$ pc. We repeated this process for each of the potential solutions.

7. Summary and conclusions

This study presents an asteroseismic investigation of the ZZ Ceti star WD 1310+583. A prerequisite for asteroseismic modelling is the identification of the star's normal pulsation modes. These modes were derived from 120-second cadence photometric data obtained with the Transiting Exoplanet Survey Satellite (TESS), supplemented by relevant parameters available in the literature.

Additional constraints were provided by spectroscopic analysis, based on data collected with the Cosmic Origins Spectrograph onboard the Hubble Space Telescope. We also examined the possible presence of rotationally split multiplets.

The asteroseismic modelling yielded a best-fit model characterised by the following physical parameters: $M_* = 0.632\,M_\odot$, $T_{\rm eff}$ = 11 702 K, being that stellar mass compatible with the predictions of the period spacing ($M_\star \gtrsim 0.6 M_\odot$). The corresponding asteroseismic distance (27.75 pc) is in good agreement with the geometric distance inferred from Gaia astrometry (30.79 pc).

This work thus demonstrates the pathway from TESS light curves to the derivation of fundamental stellar parameters. Our case study highlights the suitability of TESS photometry for asteroseismic investigations, particularly for pulsators exhibiting rich frequency spectra. Continued operation of the mission will enable not only similar in-depth case studies but also ensemble analyses of white dwarf pulsators and the discovery of new compact variables.

Acknowledgements. The authors acknowledge Sam Barber and Michael H. Montgomery (Department of Astronomy, University of Texas at Austin; McDonald Observatory, Fort Davis) for their useful early discussions. The authors also acknowledge Mukremin Kilic (Homer L. Dodge Department of Physics and Astronomy, University of Oklahoma) and Antoine Bedard (Department of Physics, University of Warwick) for their helpful discussion. ZsB and ÁS acknowledge the financial support of the KKP-137523 'SeismoLab' Élvonal grant of the Hungarian Research, Development and Innovation Office (NKFIH). M.U. gratefully acknowledges support from the Research Foundation Flanders (FWO) through a Junior Postdoctoral Fellowship (grant agreement No: 1247624N). This paper includes data collected with the TESS mission, obtained from the MAST data archive at the Space Telescope Science Institute (STScI). Funding for the TESS mission is provided by the NASA Explorer Program. STScI is operated by the Association of Universities for Research in Astronomy, Inc., under NASA contract NAS 5–26555.

References

Ahumada, R., Allende Prieto, C., Almeida, A., et al. 2020, ApJS, 249, 3
Althaus, L. G., Córsico, A. H., Isern, J., & García-Berro, E. 2010, A&A Rev., 18, 471
Bailer-Jones, C. A. L., Rybizki, J., Fouesneau, M., Demleitner, M., & Andrae, R. 2021, VizieR Online Data Catalog: Distances to 1.47 billion stars in Gaia EDR3 (Bailer-Jones+, 2021), VizieR On-line Data Catalog: I/352. Originally published in: 2021AJ....161..147B
Bédard, A., Bergeron, P., Brassard, P., & Fontaine, G. 2020, ApJ, 901, 93
Bell, K. J., Córsico, A. H., Bischoff-Kim, A., et al. 2019, A&A, 632, A42
Bell, K. J., Hermes, J. J., Bischoff-Kim, A., et al. 2015, ApJ, 809, 14
Bell, K. J., Hermes, J. J., Montgomery, M. H., et al. 2016, ApJ, 829, 82
Bell, K. J., Hermes, J. J., Montgomery, M. H., et al. 2017, in Astronomical Society of the Pacific Conference Series, Vol. 509, 20th European White Dwarf Workshop, ed. P.-E. Tremblay, B. Gaensicke, & T. Marsh, 303
Bognár, Z., Kalup, C., Sódor, Á., Charpinet, S., & Hermes, J. J. 2018, MNRAS, 478, 2676
Bognár, Z., Kawaler, S. D., Bell, K. J., et al. 2020, A&A, 638, A82
Bognár, Z., Sódor, Á., Clark, I. R., & Kawaler, S. D. 2023, A&A, 674, A204
Brickhill, A. J. 1991, MNRAS, 251, 673
Calcaferro, L. M., Córsico, A. H., Uzundag, M., et al. 2024, A&A, 691, A194
Chambers, K. & Pan-STARRS Team. 2018, in American Astronomical Society Meeting Abstracts, Vol. 231, American Astronomical Society Meeting Abstracts #231, 102.01
Córsico, A. H. 2020, Frontiers in Astronomy and Space Sciences, 7, 47
Córsico, A. H. & Althaus, L. G. 2006, A&A, 454, 863
Córsico, A. H., Althaus, L. G., Miller Bertolami, M. M., & Kepler, S. O. 2019, A&A Rev., 27, 7
Cukanovaite, E., Tremblay, P.-E., Bergeron, P., et al. 2021, MNRAS, 501, 5274
Dolez, N. & Vauclair, G. 1981, A&A, 102, 375
Fontaine, G. & Brassard, P. 2008, PASP, 120, 1043
Gentile Fusillo, N. P., Tremblay, P. E., Cukanovaite, E., et al. 2021, MNRAS, 508, 3877
Gentile Fusillo, N. P., Tremblay, P. E., Jordan, S., et al. 2018, MNRAS, 473, 3693
Goldreich, P. & Wu, Y. 1999, ApJ, 511, 904
Handler, G., Pikall, H., O'Donoghue, D., et al. 1997, MNRAS, 286, 303
Hermes, J. J., Montgomery, M. H., Bell, K. J., et al. 2015, ApJ, 810, L5
Kawaler, S. D. 1988, in IAU Symposium, Vol. 123, Advances in Helio- and Asteroseismology, ed. J. Christensen-Dalsgaard & S. Frandsen, 329
Koen, C. & Laney, D. 2000, MNRAS, 311, 636
Leggett, S. K., Bergeron, P., Subasavage, J. P., et al. 2018, ApJS, 239, 26
Munday, J., Pelisoli, I., Tremblay, P. E., et al. 2024, MNRAS, 532, 2534
O'Brien, M. W., Tremblay, P. E., Klein, B. L., et al. 2024, MNRAS, 527, 8687
O'Donoghue, D. 1994, MNRAS, 270, 222
Ricker, G. R., Winn, J. N., Vanderspek, R., et al. 2015, Journal of Astronomical Telescopes, Instruments, and Systems, 1, 014003
Sahu, S., Gänsicke, B. T., Tremblay, P.-E., et al. 2023, MNRAS, 526, 5800
Tassoul, M., Fontaine, G., & Winget, D. E. 1990, ApJS, 72, 335
Tremblay, P. E. & Bergeron, P. 2009, ApJ, 696, 1755
Tremblay, P. E., Gianninas, A., Kilic, M., et al. 2015, ApJ, 809, 148
Tremblay, P. E., Ludwig, H. G., Steffen, M., & Freytag, B. 2013, A&A, 559, A104
Uzundag, M., De Gerónimo, F. C., Córsico, A. H., et al. 2023, MNRAS, 526, 2846
Winget, D. E. & Kepler, S. O. 2008, ARA&A, 46, 157
Winget, D. E., Nather, R. E., Clemens, J. C., et al. 1991, ApJ, 378, 326
Winget, D. E., van Horn, H. M., Tassoul, M., et al. 1982, ApJ, 252, L65
Zima, W. 2008, Communications in Asteroseismology, 155, 17

[2] https://gea.esac.esa.int/archive/